Autofocus Bayesian Compressive Sensing for Multipath Exploitation in Urban Sensing

Qisong Wu, Yimin D. Zhang, Moeness G. Amin, and Fauzia Ahmad
Center for Advanced Communications, Villanova University, Villanova, PA 19085, USA

Abstract—**Exploitation of group sparsity under multipath propagation enables high-resolution ghost-free imaging in urban sensing and through-the-wall radar imaging applications. Multipath exploitation schemes typically require exact prior information of the indoor scene layout and transceiver locations to eliminate ghosts targets. Imperfections in the prior knowledge lead to performance degradation of such schemes. In this paper, a novel autofocus Bayesian compressive sensing approach is proposed for joint scene reconstruction and correction of phase errors resulted from transceiver position uncertainties. Supporting simulation results are provided to demonstrate the effectiveness of the proposed algorithm.**

Index Terms—**Through-the-wall radar imaging, autofocus, multipath exploitation, Bayesian compressive sensing.**

I. INTRODUCTION

A major challenge in urban sensing and through-the-wall radar imaging (TWRI) is the presence of multipath. Multipath returns originate from reflections of electromagnetic (EM) waves off the targets of interest in conjunction with the building walls, floor, and/or ceiling. Such secondary reflections gives rise to false targets or "ghosts" at positions other than those of the actual targets, which clutter the imaged scene and compromise target detection [1–5]. If precise knowledge of the room layout and transceiver locations is available *a priori*, the multipath returns can be exploited to improve the imaging performance [6–9]. However, as the transceivers are often hand-held or mounted on moving platforms, it is inevitable to introduce transceiver location errors in practical operational scenarios. Therefore, it is imperative to develop autofocus multipath exploitation techniques that can provide accurate imaging in the presence of location uncertainties.

Various studies have been presented for autofocus problems in radar imaging applications. One of the most well-known techniques, i.e., phase gradient autofocus (PGA) [10], estimates the phase error using the data obtained by isolating many single defocused targets via center-shifting and windowing operations. It is based on the assumption that there exist prominent scatterers in the range cell. An alternate technique is based on the optimization of a sharpness metric of the defocussed image intensity [11, 12]. However, these conventional techniques are invalid in TWRI, because it is difficult to distinguish the ghost targets from the true targets, especially when the targets of interest are stationary. Recently developed compressive sensing (CS) based autofocus approaches [13, 14] form a different class of effective tools for sparse signal reconstruction in the presence of phase errors. Both approaches, which introduce a diagonal matrix to model the phase errors, involve an iterative scheme including consecutive steps of sparse signal recovery and phase error estimation.

In this paper, inspired by [13, 14], a novel autofocus Bayesian compressive sensing (ABCS) scheme is proposed to achieve high-resolution imaging with multipath exploitation in the presence of uncertain transceiver locations in TWRI. To the best of our knowledge, autofocus imaging with multipath exploitation has not been investigated previously. We first develop a forward model under multipath propagation in the presence of imperfect transceiver locations.

It is observed that the phase errors generally differ across multipath propagations, whereas all the pixels share similar phase errors in each path, due to the relative large propagation distance and finite size of the region of interest. Based on this forward model, a novel autofocus imaging approach is proposed to jointly acquire high-resolution image reconstruction and implement the phase error corrections within the nonparametric sparse Bayesian learning framework. Simulation results verify the effectiveness of the forward model and superiority of the proposed ABCS method.

Notations: We use lower-case (upper-case) bold characters to denote vectors (matrices). $p(\cdot)$ denotes the probability density function (pdf). $\mathcal{CN}(x|a,b)$ represents a random variable x that follows a complex Gaussian distribution with mean a and variance b, and $\mathrm{U}(x|a,b)$ describes that random variable x is uniform distributed between a and b. $\lceil x/y \rceil$ denotes the modulus after x over y, and $\lfloor x/y \rfloor$ denotes the remainder after x over y. In addition, $(\cdot)^T$ and $(\cdot)^H$, respectively, denote transpose and conjugate transpose of a matrix or vector, $\mathbf{I}_N$ denotes the $N \times N$ identity matrix. "$\odot$" and "$\otimes$" denote element-wise (Hadamard) and kronecker multiplication, respectively. $\mathrm{Im}(x)$ and $\mathrm{Re}(x)$ are respectively the imaginary and real components of x.

II. SIGNAL MODEL

We assume monostatic stepped-frequency radar operation [3] and consider a few stationary targets enclosed by two side walls and a back wall. For simplicity, the front wall is ignored. Extensive studies are available on the parameter estimation and compensation of the front wall [1, 15, 16]. A wideband transceiver is mounted on a vehicle moving parallel to the x-axis at downrange y_0 to synthesize an N-element aperture, and transmits a stepped-frequency signal consisting of M frequencies at each position. The M frequencies, f_m, $m \in \{1, \cdots, M\}$, are uniformly spaced over the signal bandwidth B. Under monostatic operation, the target returns can be expressed in baseband as [8],

$$y(m,n) = \sum_{l=1}^{N_x N_y} w_l \exp(-j2\pi \frac{r_{ln}}{\lambda_m}), \qquad (1)$$

$$r_{ln} = 2\sqrt{(x_l - x_n)^2 + (y_l - y_0)^2}, \qquad (2)$$

where N_x and N_y, respectively, denote the number of pixels in crossrange and downrange within the region of interest, r_{ln} represents the round-trip propagation distance between the lth scatterer and nth transceiver position, w_l is the complex reflectivity corresponding to the lth pixel, and $\lambda_m = f_m/c$ with c being the speed of light. The location of the nth synthetic aperture position is denoted by (x_n, y_0).

The measurement data vector $\mathbf{y} = [y(1,1), \cdots, y(M,N)]^T \in \mathcal{C}^{MN}$ is obtained by stacking all measurements $y(m,n)$ into a single column vector, i.e.,

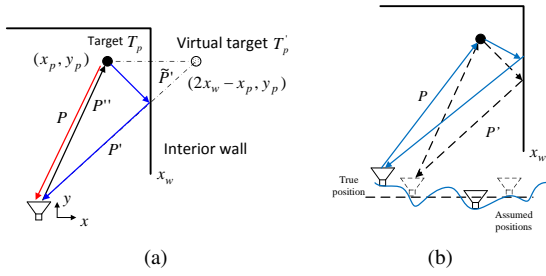$$\mathbf{y} = \mathbf{D}\mathbf{w}, \qquad (3)$$

Fig. 1: (a) Multipath propagations via reflections at interior walls. (b) Multipath propagation with transceiver position errors.

with the (i,l)th element of the sensing matrix $\mathbf{D} \in \mathcal{C}^{MN \times N_x N_y}$ given by

$$[\mathbf{D}]_{il} = \exp\left(-j2\pi \frac{r_{ln}}{\lambda_m}\right) \tag{4}$$

for $i \in \{1, \cdots, MN\}$, $m = \lceil i/M \rceil$, and $n = \lfloor i/N \rfloor$, and $\mathbf{w} \in \mathcal{C}^{N_x N_y}$ represents the target reflectivity vector. Note that most of elements in $\mathbf{w}$ are zero due to limited spatial occupancies in practice. As such, CS can be used for sparse signal reconstruction.

A. Interior Wall Multipath

The transmitted signal may reach the target via reflections at one or more secondary reflectors (typically an interior wall), as depicted in Fig. 1(a). Assuming one direct path and a maximum of $K-1$ multipath returns, the forward model under multipath propagation can be expressed as [8],

$$\mathbf{y} = \mathbf{D}_0 \mathbf{w}_0 + \mathbf{D}_1 \mathbf{w}_1 + \cdots + \mathbf{D}_{K-1} \mathbf{w}_{K-1}, \tag{5}$$

where $\mathbf{D}_0 \in \mathcal{C}^{MN \times N_x N_y}$ and $\mathbf{w}_0 \in \mathcal{C}^{N_x N_y}$, respectively, denote the sensing matrix and complex reflectivities for the direct path (defined in eqs. (3) and (4)), while $\mathbf{D}_k$ and $\mathbf{w}_k$ with $k \in \{1, \cdots K-1\}$ are the respective sensing matrix and the complex reflectivities corresponding to the kth multipath. The elements of $\mathbf{D}_k, k \in \{1, \cdots K-1\}$, are phase terms, analogous to (4), which incorporate the propagation distances associated with the kth multipath return. Assuming knowledge of the room geometry, these distances can be readily computed from geometric considerations [7, 8]. The target reflectivity vectors $\mathbf{w}_k, k = 0, ..., K-1$, share a common support, i.e., they have the same respective positions of nonzero entries, although the exact values of the reflectivity coefficients generally differ [8].

B. Multipath Propagation with Uncertain Transceiver Positions

Assuming $(\Delta x_n, \Delta y_n)$ to be the uncertainties in the nth transceiver position, the propagation distance between the nth transceiver and the lth scatterer for the direct path is expressed as,

$$\tilde{r}_{ln} = 2\sqrt{(x_l - x_n - \Delta x_n)^2 + (y_l - y_0 - \Delta y_n)^2}$$
$$\approx r_{ln} - 2\sin\theta_{ln}\Delta x_n - 2\cos\theta_{ln}\Delta y_n$$
$$= r_{ln} - 2\Delta r_n \sin(\theta_{nl} + \Delta\theta_n), \tag{6}$$
$$\Delta r_n = \sqrt{\Delta x_n^2 + \Delta y_n^2}, \quad \Delta\theta_n = \arccos(\Delta x_n/\Delta r_n), \tag{7}$$

where $2\Delta r_n \sin(\theta_{nl} + \Delta\theta_n)$ denotes the deviation from the hypothesized propagation distance r_{ln} under $\Delta x_n \ll r_{ln}$ and $\Delta y_n \ll r_{ln}$. Considering the finite room size and relatively large r_{ln}, Eq. (6) can be further approximated as,

$$\tilde{r}_{ln} \approx r_{ln} - 2\Delta r_n \sin(\theta_n + \Delta\theta_n), \tag{8}$$

where θ_n is the squint angle from the nth hypothesized transceiver position to a reference scatterer in the observed scene. The phase errors generally differ for each multipath due to the diverse propagation geometries. As such, the forward model under multipath propagation in the presence of uncertain transceiver positions is given by,

$$\mathbf{y} = \mathbf{A}_0 \mathbf{D}_0 \mathbf{w}_0 + \mathbf{A}_1 \mathbf{D}_1 \mathbf{w}_1 + \cdots + \mathbf{A}_{K-1} \mathbf{D}_{K-1} \mathbf{w}_{K-1}, \tag{9}$$

where $\mathbf{A}_k$ denotes the phase error matrix for the kth multipath, which is determined by the frequency and the path errors and is given as

$$\mathbf{A}_k = \text{diag}(\mathbf{e}_k), \quad \mathbf{e}_k = \left[e^{j\psi_1^{(k)}}, \cdots, e^{j\psi_{MN}^{(k)}}\right]^T. \tag{10}$$

C. Compressed Data Collection

Within the CS framework, we perform sparse reconstruction using only a subset of the full measurements. Mathematically, the data reduction operation can be expressed as a measurement or downsampling matrix $\mathbf{B} \in \mathcal{R}^{L \times MN}$ acting on the full measurements, where $L \ll MN$ is the number of reduced measurements. For stepped frequency radar system, a binary measurement matrix $\mathbf{B} \in \{0,1\}^{L \times MN}$ is a reasonable choice [8, 17]. As such, we acquire an undersampled measurement vector $\mathbf{s} \in \mathcal{C}^L$ as

$$\mathbf{s} = \mathbf{B}\mathbf{y} = \mathbf{E}_0 \mathbf{D}_0 \mathbf{w}_0 + \mathbf{E}_1 \mathbf{D}_1 \mathbf{w}_1 + \cdots + \mathbf{E}_{K-1} \mathbf{D}_{K-1} \mathbf{w}_{K-1} + \boldsymbol{\epsilon}, \tag{11}$$

where $\mathbf{E}_k = \mathbf{B}\mathbf{A}_k \in \mathcal{C}^{L \times MN}$. Without loss of generality, a measurement noise vector $\boldsymbol{\epsilon} \in \mathcal{C}^L$ is added to the reduced data.

III. AUTOFOCUS BAYESIAN COMPRESSIVE SENSING

A. Generative model

From (11), the following three observations are in order: 1) Direct and multipath returns may be unresolvable; 2) The reflectivity coefficients share the same sparsity pattern across multipath propagations; and 3) There exist separate phase errors for each multipath. These unique properties are utilized to propose a novel ABCS method below.

Following the sparse Bayesian learning technique, we place a hierarchical structure on $\mathbf{W} = [\mathbf{w}_0, \cdots, \mathbf{w}_{K-1}]$ to encourage group sparsity:

$$p(\mathbf{W}|\boldsymbol{\alpha}) = \prod_{i=1}^{N_x N_y} \mathcal{CN}\left(\mathbf{w}_{i\cdot}|, \mathbf{0}, \alpha_i \mathbf{I}_K\right)$$
$$= \prod_{i=1}^{N_x N_y} \prod_{k=0}^{K-1} \mathcal{CN}\left(w_{ki}|0, \alpha_i\right), \tag{12}$$

where $\mathbf{w}_{i\cdot} = [w_{i,0}, \cdots, w_{i,K-1}] \in \mathcal{C}^{1 \times K}$ is the reflectivity coefficient collection corresponding to the ith scatterer across the K propagation paths, and α_i is the variance shared by each element of $\mathbf{w}_{i\cdot}$. When α_i approaches zero, its corresponding element in $\mathbf{w}_{i\cdot}$ will approach zero and be pruned away from the model.

To promote sparsity over the reflectivity coefficients $\mathbf{w}_{i\cdot}$, a Gamma prior is placed on α_i^{-1} [18], i.e.,

$$\alpha_i^{-1} \sim \text{Gamma}(\alpha_i^{-1}|a,b), \tag{13}$$

where

$$\text{Gamma}(x^{-1}|a,b) = \Gamma(a)^{-1} b^a x^{-(a-1)} e^{-\frac{b}{x}}, \tag{14}$$

and $\Gamma(\cdot)$ denotes the Gamma function.

Without loss of generality, a complex Gaussian prior is placed on the additive measurement noise, i.e.,

$$\boldsymbol{\epsilon} \sim \mathcal{CN}(\boldsymbol{\epsilon}|0, \beta_0), \tag{15}$$

where β_0 is the noise variance. Similar to $\boldsymbol{\alpha}$, we place β_0^{-1} on the Gamma prior with parameters c and d. We use $a = b = c = d = 0$ as a default choice [18].

A noninformative prior is placed on the stochastic error phase as

$$\psi_l^{(k)} \sim \mathrm{U}\left(\psi_l^{(k)}\Big|0, 2\pi\right), \tag{16}$$

with $k \in [1, \cdots, K]$ and $l \in [1, \cdots, L]$.

According to the Bayesian theorem, the posterior distribution can be expressed as,

$$p\left(\bar{\mathbf{w}}, \boldsymbol{\alpha}, \beta_0, \boldsymbol{\Psi} \,|\, \mathbf{s}\right) = \frac{p(\mathbf{s}|\bar{\mathbf{w}}, \boldsymbol{\Psi}, \beta_0)p(\bar{\mathbf{w}}|\boldsymbol{\alpha})p(\boldsymbol{\alpha})p(\beta_0)p(\boldsymbol{\Psi})}{p(\mathbf{s})}, \tag{17}$$

where $\bar{\mathbf{w}} = [\mathbf{w}_{1\cdot}^T, \cdots, \mathbf{w}_{N_x N_y\cdot}^T] \in \mathcal{C}^{K N_x N_y}$ is an aligned reflectivity coefficient vector, and $\boldsymbol{\Psi} = [\mathbf{e}_0, \cdots, \mathbf{e}_{K-1}] \in \mathcal{C}^{L \times K}$. The computation of $p(\mathbf{s})$ is often intractable due to the multidimensional integral. We introduce a Monte Carlo Markov Chain (MCMC) method to perform the posterior inference [19].

B. Bayesian Inference Based on MCMC

In this section, we perform the posterior inference based on the MCMC sampling scheme, which suggests an iteration procedure. We can acquire analytical posterior distribution of $\mathbf{W}$, given other parameters $\{\boldsymbol{\alpha}, \beta_0, \boldsymbol{\Psi}\}$, due to the conjugacy. The effective bound optimization technique is introduced to perform the point estimation for $\boldsymbol{\alpha}$ and β_0. The phase error can be estimated by the maximum a posterior (MAP) technique.

1) Updating $\bar{\mathbf{w}}$: The posterior distribution of $\bar{\mathbf{w}}$ can be analytically obtained due to the conjugate property. Given $\boldsymbol{\alpha}$, β_0 and $\boldsymbol{\Psi}$, we have

$$\mathbf{w}_{i\cdot} \sim \mathcal{CN}(\mathbf{w}_{i\cdot}\,|\,\boldsymbol{\mu}_{i\cdot}, \boldsymbol{\Sigma}_i), \quad 1 \leq i \leq N_x N_y, \tag{18}$$

$$\boldsymbol{\mu}_{i\cdot} = \beta_0^{-1}\boldsymbol{\Sigma}_i\tilde{\mathbf{D}}_i^H\mathbf{s}, \tag{19}$$

$$\boldsymbol{\Sigma}_i = \left(\beta_0^{-1}\tilde{\mathbf{D}}_i^H\tilde{\mathbf{D}}_i + \alpha_i^{-1}\mathbf{I}_K\right)^{-1}, \tag{20}$$

$$\tilde{\mathbf{D}}_i = [\mathbf{E}_0\mathbf{d}_{0,i}, \cdots, \mathbf{E}_{K-1}\mathbf{d}_{K-1,i}], \tag{21}$$

where $\tilde{\mathbf{D}}_i \in \mathcal{C}^{L \times K}$ denotes the collection of the ith column across the K matrices $\{\mathbf{E}_k\mathbf{D}_k\}_{k=0}^{K-1}$, and $\mathbf{d}_{k,i}$ is the ith column in $\mathbf{D}_k$.

2) Updating $\boldsymbol{\alpha}$ and β_0: With known $\boldsymbol{\alpha}$ and β_0, the mean and covariance of each scattering coefficient are respectively derived in (19) and (20). The associated *learning* problem, thus, becomes a search for the parameters $\boldsymbol{\alpha}$ and β_0. The empirical Bayesian estimate for $\boldsymbol{\alpha}$ and β_0 is determined by maximizing the marginal likelihood, or equivalently, its logarithm,

$$\{\boldsymbol{\alpha}, \beta_0\} = \underset{\boldsymbol{\alpha}, \beta_0}{\mathrm{argmax}}\ \mathcal{L}(\boldsymbol{\alpha}, \beta_0) \tag{22}$$

where

$$\mathcal{L}(\boldsymbol{\alpha}, \beta_0) = \sum_{l=1}^{L}\log p(\mathbf{s}|\boldsymbol{\alpha}, \beta_0) = \int p(\mathbf{s}|\bar{\mathbf{w}}, \beta_0)p(\bar{\mathbf{w}}|\boldsymbol{\alpha})d\bar{\mathbf{w}}$$

$$\equiv -[\log|\mathbf{C}| + \mathbf{s}^H\mathbf{C}^{-1}\mathbf{s}],$$

$$\mathbf{C} = \beta_0\mathbf{I}_L + \bar{\mathbf{D}}(\mathbf{A} \otimes \mathbf{I}_K)\bar{\mathbf{D}}^H, \tag{23}$$

$$\bar{\mathbf{D}} = [\tilde{\mathbf{D}}_1, \cdots, \tilde{\mathbf{D}}_{N_x N_y}], \tag{24}$$

in which $\mathbf{C} \in \mathcal{C}^{L \times L}$, and $\bar{\mathbf{D}} \in \mathcal{C}^{L \times K N_x N_y}$ with $L \ll K N_x N_y$. A type-II maximum likelihood (ML) approximation [20] employs the point estimates for β_0 and $\boldsymbol{\alpha}$ to maximize (22), which can be implemented via the expectation maximization (EM) algorithm. However, the method based on EM technique has slow convergence [18]. Several effective approaches have been proposed to speed up the convergence [18, 21, 22]. It is proved that the approach based on the

bound optimization technique (known as Majorization-Minimization method) can be used to achieve better sparse solutions [22–24].

In this paper, we derive $\boldsymbol{\alpha}$ by following the bound optimization technique. We use the supporting hyperplane of the second term $\log|\mathbf{C}|$ in (23). Let $\boldsymbol{\alpha}^*$ be a given point in the $\boldsymbol{\alpha}$-space. Then,

$$\mathcal{L}(\boldsymbol{\alpha}) \triangleq \log|\mathbf{C}| = \log|\beta_0\mathbf{I}_L + \bar{\mathbf{D}}(\mathbf{A} \otimes \mathbf{I}_K)\bar{\mathbf{D}}^H|$$

$$\leq \log|\mathbf{C}^*| + \sum_{i=1}^{N_x N_y} \mathrm{Tr}\left[(\mathbf{C}^*)^{-1}\tilde{\mathbf{D}}_i\tilde{\mathbf{D}}_i^H\right](\alpha_i - \alpha_i^*)$$

$$\triangleq \tilde{\mathcal{L}}(\boldsymbol{\alpha}), \tag{25}$$

where

$$\mathbf{C}^* = \beta_0\mathbf{I}_L + \bar{\mathbf{D}}(\mathbf{A}^* \otimes \mathbf{I}_K)\bar{\mathbf{D}}^H, \tag{26}$$

$$\mathbf{A}^* = \mathrm{diag}(\alpha_1^*, \cdots, \alpha_{N_x N_y}^*). \tag{27}$$

Note that the function $\tilde{\mathcal{L}}(\boldsymbol{\alpha})$ defined in (25) is convex over $\boldsymbol{\alpha}$ and, when $\boldsymbol{\alpha} = \boldsymbol{\alpha}^*$, we have $\mathcal{L}(\boldsymbol{\alpha}^*) = \tilde{\mathcal{L}}(\boldsymbol{\alpha}^*)$. Further, for any $\boldsymbol{\alpha}_{\min}$ which minimizes $\tilde{\mathcal{L}}(\boldsymbol{\alpha})$, we have $\mathcal{L}(\boldsymbol{\alpha}_{\min}) \leq \tilde{\mathcal{L}}(\boldsymbol{\alpha}_{\min}) \leq \tilde{\mathcal{L}}(\boldsymbol{\alpha}^*)$ [23]. Furthermore, based on the identity property, we have a surrogate function for the third term in (23), expressed as

$$\mathbf{s}^H\mathbf{C}^{-1}\mathbf{s} \equiv \min_{\bar{\mathbf{w}}} \beta_0^{-1}\|\mathbf{s} - \bar{\mathbf{D}}\bar{\mathbf{w}}\|_2^2 + \bar{\mathbf{w}}^H(\mathbf{A}^{-1} \otimes \mathbf{I}_K)\bar{\mathbf{w}}. \tag{28}$$

Substituting (25) and (28) in (23), we can define a new function as

$$\mathcal{G}(\boldsymbol{\alpha}, \bar{\mathbf{w}}) \triangleq \beta_0^{-1}\|\mathbf{s} - \sum_{i=1}^{N_x N_y}\tilde{\mathbf{D}}_i\mathbf{w}_{i\cdot}^T\|_2^2 + \sum_{i=1}^{N_x N_y}\alpha_i^{-1}\mathbf{w}_{i\cdot}\mathbf{w}_{i\cdot}^H$$

$$+ \log|\mathbf{C}^*| + \sum_{i=1}^{N_x N_y}\mathrm{Tr}\left[(\mathbf{C}^*)^{-1}\tilde{\mathbf{D}}_i\tilde{\mathbf{D}}_i^H\right](\alpha_i - \alpha_i^*). \tag{29}$$

It is important to note that $\mathcal{G}(\boldsymbol{\alpha}, \bar{\mathbf{w}})$ is convex in both $\{\mathbf{w}_{\cdot i}\}_{i=1,L}$ and $\boldsymbol{\alpha}$. It is easily shown that the solution $\boldsymbol{\alpha}$ of $\tilde{\mathcal{L}}(\boldsymbol{\alpha})$ in (25) is the solution $\{\mathbf{w}_{i\cdot}\}_{i=1,L}$ of $\mathcal{G}(\boldsymbol{\alpha}, \bar{\mathbf{w}})$ in (29). Thus, $\mathcal{G}(\boldsymbol{\alpha}, \bar{\mathbf{w}})$ is our final cost function.

Setting the derivative of $\mathcal{G}$ with respect to α_i to zero, we obtain

$$\alpha_i^{(\mathrm{new})} = \sqrt{\frac{\mathbf{w}_{i\cdot}\mathbf{w}_{i\cdot}^H}{\mathrm{Tr}\left[(\mathbf{C}^*)^{-1}\tilde{\mathbf{D}}_i\tilde{\mathbf{D}}_i^H\right]}}. \tag{30}$$

It is proved that the updated formulation in (30) based on this bound optimization technique requires far fewer iterations than the one used in the EM algorithm [18, 22, 23]. We acquire the closed-form $\boldsymbol{\alpha}$ by solving a surrogate convex function. Furthermore, we take the derivative of (23) with respect to β_0, and acquire [18],

$$\beta_0^{(\mathrm{new})} = \frac{\|\mathbf{s} - \bar{\mathbf{D}}\bar{\mathbf{w}}^*\|_2^2 + \mathrm{Tr}(\boldsymbol{\Sigma}_0\bar{\mathbf{D}}\bar{\mathbf{D}}^H)}{L}, \tag{31}$$

$$\bar{\mathbf{w}}^* = \beta_0^{-1}\boldsymbol{\Sigma}_0\bar{\mathbf{D}}^H\mathbf{s}, \tag{32}$$

$$\boldsymbol{\Sigma}_0 = \left(\beta_0^{-1}\bar{\mathbf{D}}^H\bar{\mathbf{D}} + \mathbf{A}^{-1} \otimes \mathbf{I}_K\right)^{-1}. \tag{33}$$

3) Updating error phase $\boldsymbol{\Psi}$: The solution to the error phase $\boldsymbol{\Psi}$ can be formulated as the following maximization problem,

$$\hat{\boldsymbol{\Psi}} = \arg\max_{\boldsymbol{\Psi}}\ \log p(\mathbf{s}|\bar{\mathbf{w}}, \boldsymbol{\Psi}, \beta_0)p(\boldsymbol{\Psi})$$

$$\equiv \arg\min_{\boldsymbol{\Psi}}\ \|\mathbf{s} - \mathbf{E}_0\mathbf{D}_0\mathbf{w}_0 - \mathbf{E}_1\mathbf{D}_1\mathbf{w}_1$$

$$- \cdots - \mathbf{E}_{K-1}\mathbf{D}_{K-1}\mathbf{w}_{K-1}\|_2^2. \tag{34}$$

By taking the derivative of (34) with respect to $\boldsymbol{\Psi}$, we obtain,

$$\boldsymbol{\psi}^{(k)} = \arctan\frac{\mathrm{Im}(\overline{\mathbf{D}_k\boldsymbol{\mu}_{k\cdot}} \odot \mathbf{s}_{\backslash k})}{\mathrm{Re}(\overline{\mathbf{D}_k\boldsymbol{\mu}_{k\cdot}} \odot \mathbf{s}_{\backslash k})}, \tag{35}$$
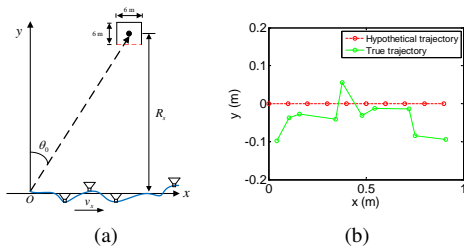
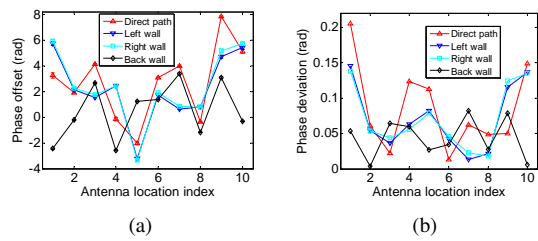Fig. 2: Simulated geometry in TWRI and motion trajectory.

Fig. 3: Average phase errors and standard deviation. (a) Errorbar plot for phase errors. (b) Standard deviations of phase error in multipath propagations

where $\boldsymbol{\mu}_{k.}$ denotes the posterior mean of the reflectivity coefficients $\mathbf{w}_k$, and $\mathbf{s}_{\backslash k}$ is the measurement data excluding the contribution from the kth propagation path.

In summary, it is observed that $\boldsymbol{\mu}$ in (19) and $\boldsymbol{\Sigma}$ in (20) are functions of $\boldsymbol{\alpha}$ in (30), β_0 in (31) and $\boldsymbol{\psi}$ in (35), and vice versa. It suggests an iterative approach, which iterates between (19), (20) and (30), (31) and (35), until a convergence criterion is satisfied.

IV. SIMULATION RESULTS

A typical TWRI scenario is simulated, as shown in Fig. 2(a). A transceiver mounted on a ground vehicle, moving at v_x=15 m/s along the x-axis, transmits and receives the stepped-frequency signal, consisting of 200 equally spaced frequency steps from 1 GHz to 2 GHz, and the pulse repetition frequency (PRF) is 150 Hz. The data collection time is one second, and thus the length of synthetic aperture is 1 m and the number of synthetic positions is 10. The origin of the coordinate system is chosen to the initial location of the transceiver. The initial squint angle is $\theta_0 = 45°$ and the size of illuminated room is 6 m × 6 m. The distance R_s from the center of room to the x-axis is 50 m. The distance between two adjacent discretized image pixels along both crossrange and downrange is 0.1 m. The received signal comprises the direct returns and the multipath returns via secondary reflections at the three interior walls, yielding a total of $K = 4$ paths. The scattering coefficients for the direct paths are drawn from $\mathcal{CN}(0, 1)$, and the signal amplitudes of the multipath returns are assumed to decay with the distance. Complex white Gaussian noise is added to the measurements with a signal-to-noise ratio (SNR) of 10 dB. Only 25% frequencies are randomly selected at each transceiver location for CS-based imaging.

The first simulation is to verify the effectiveness of the proposed forward model in Eq. (9). In the above TWRI geometry, random location errors with standard deviation of $v_x/(2\text{PRF})$ are added at each synthetic aperture position, as depcited in Fig. 2(b), which clearly shows the deviations from the hypothesized trajectory. Fig. 3(a) shows the error bar plot with means and standard deviations of phase errors in diverse multipath propagations. The average phase errors in Fig. 3(a), which are calculated based on all the pixels in the region of interest, generally differ across multipaths reflected from interior walls and transceiver locations, when the uncertain transceiver locations are used. However, the standard deviations of phase errors are much less than $\pi/4$ across multipath propagations, no matter the transceiver location, as shown in Fig. 3(b). Therefore, it is reasonable to consider the corrupted phase error in each multipath propagations in the forward model.

The second simulation is to verify the effectiveness of the proposed ABCS algorithm. The sparse scene, shown in Fig. 4(a), is considered. Figs. 4(b) and 4(c), respectively, show the reconstructed results from BOMP [25] with the true sparsity, and block sparse Bayesian learning approach (BSBL) [22], which only take the group sparsity into
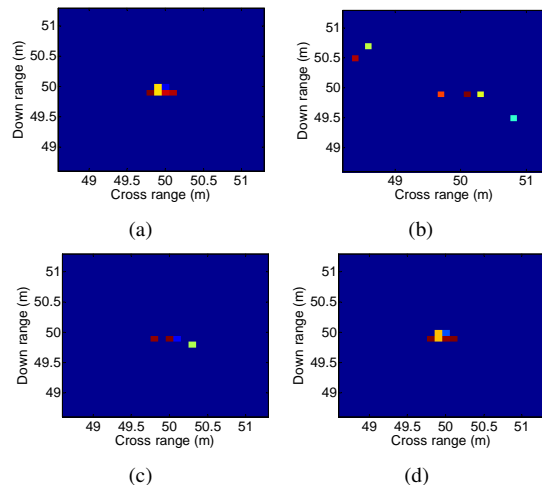

Fig. 4: Reconstructed results based on these CS approaches. (a) Original scene. (b) Result from BOMP with true sparsity. (c) Result from BSBL. (d) Result from the proposed ABCS method.

account. Due to the corrupted phase errors caused by the antenna location errors, both algorithms fail to reconstruct the sparse targets. However, by exploiting the joint sparse reconstruction and phase error correction, the proposed ABCS algorithm correctly reconstructs the sparse scene, as shown in Fig. 4(d).

V. CONCLUSION

In TWRI, compressive sensing based multipath exploitation techniques enable high-resolution imaging given accurate knowledge of the physical geometry. However, the quality of the reconstructed image degrades under imperfect prior knowledge. We have prroposed a novel autofocus Bayesian compressive sensing approach with multipath exploitation to perform through-the-wall scene reconstruction in the presence of uncertain transceiver locations. We first develop a forward model under multipath propagation, and then propose autofocus Bayesian compressive sensing algorithm to jointly reconstruct the sparse targets of interest and implement phase error correction in a nonparametric Bayesian framework. Simulation results are provided to validate the proposed forward model and reconstruction algorithm, and show superiority over conventional CS imaging techniques.

REFERENCES

[1] M. G. Amin, *Through-the-Wall Radar Imaging*. CRC Press, 2010.

[2] Y. Zhang, M. G. Amin, and F. Ahmad, "A novel approach for multiple moving target localization using dual-frequency radars and time-frequency distributions," in *Proc. Annual Asilomar Conf. Signals, Systems, and Computers*, (Pacific Grove, CA), pp. 1817–1821, Nov. 2007.

[3] F. Ahmad and M. G. Amin, "Multi-location wideband synthetic aperture imaging for urban sensing applications," *J. Franklin Inst.*, vol. 345, no. 6, pp. 618–639, 2008.

[4] T. Dogarur and C. Le, "Sar images of rooms and buildings based on fdtd computer models," *IEEE Trans. Geosci. Remote Sens.*, vol. 47, no. 5, pp. 1388–1401, 2008.

[5] R. J. Burkholder, "Electromagnetic models for exploting multipath propagation in through-wall radar imaging," in *Proc. Int. Conf. Electrmag. Adv. Appl.*, pp. 572–575, 2008.

[6] S. Kidera, T. Sakamoto, and T. Sato, "Extended imaging algorithm based on aperture synthesis with doublescattered waves for UWB radars," *IEEE Trans. Geosci. Remote Sens.*, vol. 49, no. 12, pp. 5128–5139, 2011.

[7] P. Setlur, M. Amin, and F. Ahmad, "Multipath model and exploitation in through-the-wall and urban radar sensing," *IEEE Trans. Geosci. Remote Sens.*, vol. 49, no. 10, pp. 4021–4034, 2011.

[8] M. Leigsnering, F. Ahmad, M. G. Amin, and A. M. Zoubir, "Compressive sensing based specular multipath exploitation for through-the-wall radar imaging," in *Proc. IEEE ICASSP*, (Vancouver, Canada), May 2013.

[9] Q. Wu, Y. D. Zhang, M. G. Amin, and F. Ahmad, "Through-the-wall radar imaging based on modified Bayesian compressive sensing," in *Proc. IEEE China Summit and Int. Conf. Signal and Inform. Proc.*, Xi'an, China, pp. 232-236, July 2014.

[10] D. E. Wahl, P. H. Eichel, D. C. Ghiglia, and C. V. Jakowatz, "Phase gradient autofocus-a robust tool for high resolution SAR phase correction," *IEEE Trans. Aerospace Electron. Syst.*, vol. 30, no. 3, pp. 827–835, 1994.

[11] X. Li, G. Liu, and J. Ni, "Autofocusing of ISAR images based on entropy minimization," *IEEE Trans. Aerospace Electron. Syst.*, vol. 35, no. 4, pp. 1240–1252, 1999.

[12] R. L. Morrison, M. N. Do, and D. C. Munson, "SAR image autofocus by sharpness optimization: A theoretical study," *IEEE Trans. Image Proc.*, vol. 16, no. 9, pp. 2309–2321, 2007.

[13] N. O. Onhon and M. Cetin, "A sparsity-driven approach for joint SAR imaging and phase error correction," *IEEE Trans. Image Proc.*, vol. 21, no. 94, pp. 2075–2088, 2012.

[14] L. Zhao, L. Wang, G. Bi, and L. Yang, "An autofocus technique for high-resolution inverse synthetic aperture radar imagery," *IEEE Trans. Geosci. Remote Sens.*, vol. 52, no. 10, pp. 6392–6403, 2014.

[15] G. Wang, M. G. Amin, and Y. Zhang, "A new approach for target locations in the presence of wall ambiguity," *IEEE Trans. Aerospace Electron. Syst.*, vol. 42, no. 1, pp. 301–315, 2006.

[16] F. Ahmad, Y. Zhang, and M. G. Amin, "Three-dimensional wideband beamforming for imaging through a single wall," *IEEE Geosci. Remote Sens. Lett.*, vol. 5, no. 2, pp. 176–179, 2008.

[17] A. Gurbuz, J. McClellan, and W. Scott, "Compressive sensing for subsurface imaging using ground panetrating radar," *Signal Processing*, vol. 89, no. 10, pp. 1959–1972, 2009.

[18] M. E. Tipping, "Sparse Bayesian shrinkage and selection learning and the relevance vector machine," *Journal of Machine Learning Research*, vol. 1, no. 9, pp. 211–244, 2001.

[19] C. M. Bishop, *Pattern Recognition and Machine Learning*. New York, NY: Springer, 2006.

[20] D. J. C. MacKay, "Bayesian interpolation," *Neural Comput.*, vol. 4, no. 3, pp. 415–447, 1992.

[21] S. Ji, Y. Xue, and L. Carin, "Bayesian compressive sensing," *IEEE Trans. Signal Proc.*, vol. 56, no. 6, pp. 2346–2356, 2008.

[22] Z. Zhang and B. D. Rao, "Extension of SBL algorithm for the recovery of block sparse signals with inter-block correlation," *IEEE Trans. Signal Proc.*, vol. 92, no. 7, pp. 1580–1590, 2012.

[23] P. Stoica and P. Babu, "Spice and likes: Two hyperparameter-free methods for sparse-parameter estimation," *Signal Processing*, vol. 92, no. 7, pp. 1580–1590, 2012.

[24] Q. Wu, Y. D. Zhang, M. G. Amin, and B. Himed, "Complex multitask Bayesian compressive sensing," in *Proc. IEEE ICASSP*, (Florence, Italy), May 2014.

[25] Y. C. Eldar, P. Kuppinger, and H. Bölcskei, "Block-sparse signals: Uncertainty relations and efficient recovery," *IEEE Trans. Signal Proc.*, vol. 58, no. 6, pp. 3042–3054, 2010.